Morphological analysis of pores in directionally freeze-cast titanium foams

J.L. Fife, J.C. Li, D.C. Dunand,[a] and P.W. Voorhees
Department of Materials Science and Engineering, Northwestern University, Evanston, Illinois 60208-3108

(Received 9 July 2008; accepted 16 September 2008)

Synchrotron x-ray tomography was performed on titanium foams with aligned, elongated pores, initially created by sintering directionally freeze-cast preforms using two different powder sizes. Three-dimensional reconstructions of the pore structures were analyzed morphologically using interface shape and interface normal distributions. A smaller powder size leads to more completely sintered titanium walls separating the dendritic pores, which in turn created a more compact distribution of pore shapes as well as stronger pore directionality parallel to the ice growth direction. The distribution of pore shapes is comparable to trabecular bone reported in the literature, indicating the foam's potential as a bone replacement material.

I. INTRODUCTION

Metallic foams have an interesting combination of properties, such as high specific strength and stiffness when incorporated into sandwiches and high gas permeability with high thermal conductivity. This makes them useful in low-weight structural applications, filtration, battery electrodes, and acoustic damping.[1] Titanium-based foams, in particular, also combine the advantages of outstanding mechanical strength with low density, high corrosion resistance, and surface oxide biocompatibility, which make them especially promising for use in medical implants as a bone replacement material.[2–5] Thus, it is of great interest to create titanium foams that exhibit the same aligned, elongated pore architecture as bone, which gives it both its structural and mechanical anisotropy.

Directional freeze-casting is a method that relies on directional solidification to create aligned pores in ceramics[6–10] and, recently, in titanium.[11] First, a liquid, usually water, is mixed with solid powders to make slurry. The slurry is then subjected to directional solidification so that the porous structure is determined by the growth of the solid ice crystals, rejecting the powders to the interdendritic space. After solidification, the structure is freeze-dried, sublimating the ice out of the sample, leaving large aligned, elongated pores separated by walls of lightly bound solid powders, corresponding respectively to the dendritic and interdendritic regions. These powders are then sintered to create dense walls separating the pores.

X-ray tomography has been used previously to visualize ice crystals in the fields of food science and glaciology.[12–16] For instance, directional solidification of ice into meat was studied using tomography, but the information was not used to create three-dimensional (3D) reconstructions.[16] A more comprehensive study analyzed the microstructural evolution of snow in three dimensions, over time, while holding temperature constant,[15] calculating porosity, specific surface area, anisotropy, and curvature distribution of the snow crystals. Optical and x-ray tomography have also been used to create reconstructions of soap foams and to study the individual cell shapes of the foam.[17,18] In the field of metallic foams, tomography has been used to study deformation and yield mechanisms during tensile and compressive testing and for cell size and shape characterization.[19–22]

The present study quantitatively characterizes the structure of porous titanium foams created by directional freeze-casting and sintering of titanium powders of two different sizes. The calculations are performed on 3D foams reconstructed from two-dimensional (2D) tomography data to determine pore interconnectivity, inverse surface area per unit volume, pore volume fraction, interface shape distributions, as well as interface normal distributions. This analysis is useful both for understanding the structure of the metallic foam and how it compares to bone, and for investigating the dendritic solidification of water slurries. To our knowledge, it is the first time these characterization techniques have been used to study metallic foams produced using directional freeze-casting.

II. EXPERIMENTAL PROCEDURE

Unalloyed titanium powder with an average particle size of <20 μm was procured from Atlantic Equipment Engineers (Bergenfield, NJ) and will be referred to as the coarse powder. Unalloyed titanium powder with average particle size of 10 μm was purchased from

[a]Address all correspondence to this author.
e-mail: dunand@northwestern.edu
DOI: 10.1557/JMR.2009.0023

Phelly Materials Inc. (Bergenfield, NJ) and will be referred to as the fine powder. Titanium foam is created from each of these powders using the directional freeze-casting process.

The 22 vol% Ti slurry is made by mixing 3.9 g of titanium powder with 3 mL of vacuum degassed water containing 0.2 wt% agar (Eden Foods, Inc., Clinton, MI). Agar is used as a binder preventing powder collapse after ice removal. The slurry is then poured into a cylindrical glass vessel with an inner diameter of 13 mm, a height of 38 mm, and a thickness of approximately 1 mm. The vessel is placed in a freezer, with its flat, bottom surface in direct contact with a copper block, which has been cooled to 268 K. All other surfaces of the vessel are insulated with polystyrene foam to induce directional solidification of the slurry. The vessel is kept in the freezer for at least 3 h to ensure complete solidification of the ice. Experimental measurement of the average solid–liquid interface growth velocity is 3.0 ± 0.2 μm/s ($n = 3$).

The ice in the solidified ice/titanium billet is then sublimated under a 7.4 Pa vacuum at 233 K for 24 h. This resulted in a porous titanium powder preform, which is sintered under vacuum (<5.6×10^{-6} Torr) at 1273 K for 2 h and then at 1423 K for 7.75 h. From the two resulting foams, one from each powder size, approximately rectangular specimens, 4 mm × 4 mm × 8 mm, are cut in preparation for tomography. The specimen is taken from the center of the billet, approximately 1 cm from the top and bottom surfaces. Multiple specimens are cut from this area, such that the tomography specimen does not contain any of the billets' original outside surfaces and far from the cylindrical billet surfaces. A total of 5 × 9 = 45 contiguous 300× magnification optical micrographs are used to determine pore size in material adjacent to the tomography samples.

The x-ray tomography is performed at the Advanced Photon Source (APS), at the DND-CAT 5BMC beamline at Argonne National Laboratory (Argonne, IL). A bending magnet is used to deliver the synchrotron x-ray beam at energy of 45 keV. The x-ray image is created on a cryo-cooled charge-coupled device (CCD) camera through a 4× objective. A resolution of 6 μm/pixel is used, which creates a 7 mm objective. The tomography reconstructions are then carried out on a 16-node Linux cluster using filtered back-projection techniques. These 2D images are then segmented to create binary images, and 3D reconstructions are generated and used for the quantitative measurements.

After tomography, the specimen closed porosity is determined by helium pycnometry. The total porosity is determined using the Archimedes method, which is performed in deionized water after coating the sample in a thin layer of grease to prevent water infiltration. From these two porosity values, the open porosity is calculated.

III. ANALYSIS

The inverse surface area per unit volume, S_v^{-1}, of the 3D microstructure is used as the characteristic length scale. Once the reconstruction is generated, the surface area per unit volume, S_v, is calculated as the sum of the interfacial surface patches divided by the total volume of the reconstruction. The inverse of this value is taken to provide an average length scale of the structure (in micrometers).

Furthermore, the surface can be completely characterized by its two principal radii of curvature, R_1 and R_2. The principal curvatures, κ_1 and κ_2, are inversely related to the principal radii of curvature. These principal curvatures form the diagonal elements in the 2 × 2 curvature tensor matrix, which has two important invariants: the mean and Gaussian curvatures. The mean curvature, H, is defined as half the sum of the two principal curvatures:

$$H = \left(\frac{\kappa_1 + \kappa_2}{2}\right) = \frac{1}{2}\left(\frac{1}{R_1} + \frac{1}{R_2}\right) \quad . \tag{1}$$

The Gaussian curvature, K, is the product of the two principal curvatures:

$$K = \kappa_1 \kappa_2 = \frac{1}{R_1 R_2} \quad . \tag{2}$$

Both mean and Gaussian curvatures are necessary to fully define interface evolution.[23] For example, a flat interface and a saddle-shaped interface both have a mean curvature of zero but differ in Gaussian curvatures. Thus, once the 3D reconstructions are created, the mean and Gaussian curvatures are calculated using the mixed finite element/finite volume method established by Guillaume et al.[24] Then, κ_1 and κ_2 are calculated from Eqs. (3) and (4) as

$$\kappa_1 = H - \sqrt{H^2 - K} \quad . \tag{3}$$

$$\kappa_2 = H + \sqrt{H^2 - K} \quad . \tag{4}$$

The curvature data is then viewed as a 2D probability density map or interface shape distribution (ISD).[25] Let $P(\kappa_1, \kappa_2)$ be a probability density function, where $P(\kappa_1, \kappa_2) d\kappa_1 d\kappa_2$ is the probability that any interface patch chosen at random will have principal curvatures, κ_1 and κ_2, between $\kappa_1 + d\kappa_1$ and $\kappa_2 + d\kappa_2$. This probability is then displayed as a 2D probability contour plot, which is a measure of the probability of finding a patch of interface in the microstructure with a given set of principal curvatures, κ_1 and κ_2. It is divided into four regions, as illustrated in Fig. 1.

We quantify the directionality in the structures by determining the probability of finding an interface normal, **n**, in a given direction.[26] This probability is determined by projecting a given unit interface normal onto a plane tangent to the sphere and perpendicular to the

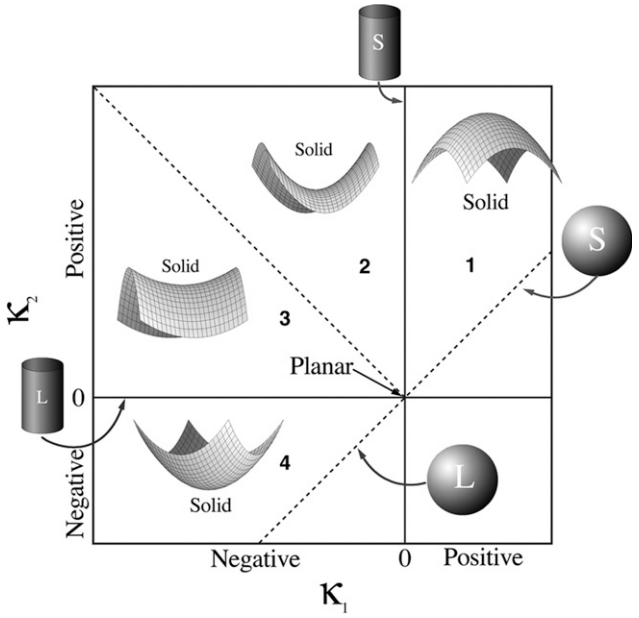

FIG. 1. Map of the local interface shapes possible in an interface shape distribution.[25] In this case, solid represents the pores and liquid represents the titanium.

projection axis. The normals originate in the center of the sphere and end on the surface of the sphere. The data is binned prior to the projection, which removes potential artifacts from binning after the projection is complete, as is typical of 2D polar plots. Thus, each bin encompasses the same 3D area of the sphere, and as a result, a contour plot of the probability distributions of interface normal orientations is created.[26]

Because experimental data is most often asymmetric, there are two views generated: a near-hemisphere and a far-hemisphere. The near-hemisphere view represents the normals along the positive axis, and the far-hemisphere view represents the normals along the negative axis with the center of the sphere at the origin. The two plots should appear qualitatively similar with the peak probability contained on one of the two plots. The peak location indicates the hemisphere that should be used to represent the structure, regardless of the direction of the projection.

There are also two types of projections used in interface normal distributions (INDs): equal-area and stereographic. Equal-area projections enhance features near the center of the plot, while stereographic projections enhance features at the edges of the plot. In this work, stereographic projections are used.

IV. RESULTS AND DISCUSSION

Figure 2 shows optical micrographs of polished cross sections of the two samples. Surfaces parallel to the freezing direction clearly show aligned, elongated pores, resulting from the growth of ice dendrites during the directional freeze-casting process. These will be referred to as macropores. Surfaces perpendicular to the freezing direction indicate that the ice dendrites grow as plates, not as needles, as expected from literature.[8,27,28] The plates show various orientations in the plane, although there are small groups of parallel plates corresponding to grains, indicating there is no preferred growth orientation for the ice crystals in the plane perpendicular to the main ice growth direction that is visible in two dimensions. Because the pores are planar, there is one dimension in which the pores are much smaller, and this dimension is used for the pore width measurements.

Visual comparison of the micrographs for the two foams with two different powder sizes shows that while there is variation within each image, the foam made from the fine powders seems to have narrower macropores. Measurements on cross sections reveal that the fine- and coarse-powder foams have pore widths of approximately 50 and 61 μm, respectively. In addition to the macropores caused by the ice dendrites, micropores are visible in the titanium walls in all four images. These micropores are due to incomplete sintering between the individual titanium powders. In addition to causing micropores, incomplete sintering leads to surface roughness on the titanium walls, as illustrated in Fig. 3, where individual titanium powders are clearly visible. The inset of Fig. 3 shows necks between two adjacent titanium powders, a clear indication of incomplete sintering.

Helium pycnometry measurements reveal both samples have zero closed porosity to within the large experimental error due to the small sample size: 3.2 ± 5.5% and 1.6 ± 6.0%, for the fine- and coarse-powder billets, respectively. The total porosities, measured by the Archimedes method, for the fine- and coarse-powder billets are 41.4 ± 0.8% and 44.6 ± 0.6%, respectively, and are assumed to be fully open.

Figure 4 shows the 3D reconstructions of the two foams. It is apparent that the reconstructed cross sections visible in Fig. 4 are generally similar to the experimental 2D optical micrographs of cross sections shown in Fig. 2. However, while the dendritic macropores are well captured by the reconstruction, the micropores are poorly represented; this is expected because the spatial resolution of the structure is 6 μm/pixel. Ideally, any feature should be represented by no less than five pixels; thus, features such as the micropores that are less than 30 μm are poorly or not at all resolved. From Figs. 2 and 3, it is clear that the micropores in each foam are on the order of the initial titanium powder sizes, and thus either too small to be reconstructed, or on the same order of the resolution, so that they are represented in the reconstruction, but likely not accurately. Nevertheless, these reconstructions are, to our knowledge, the first rendering of directionally freeze-cast foam structures in three dimensions and provide new insights into the structure of the highly anisotropic macropores produced by the ice dendrites.

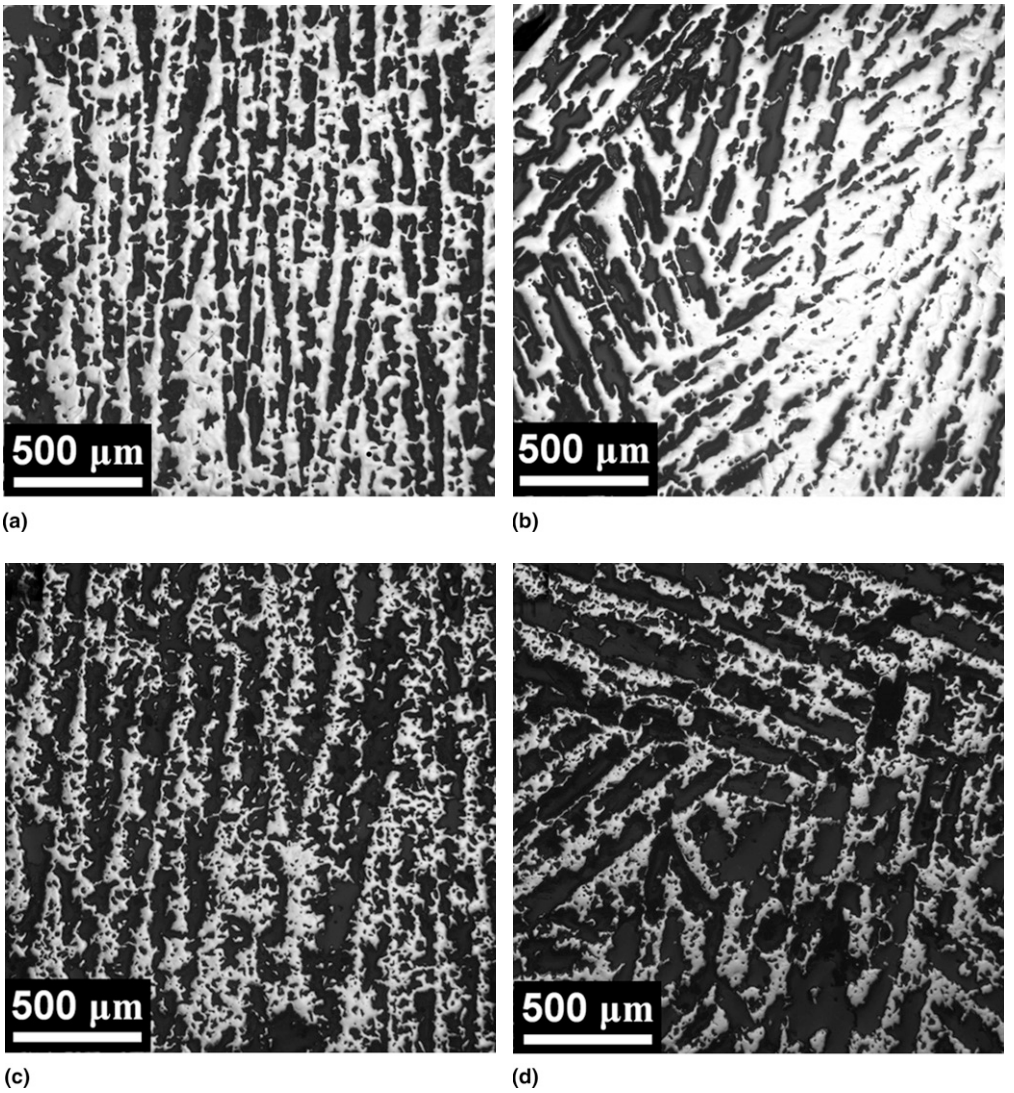

FIG. 2. Optical micrographs of titanium foams: (a, b) for fine powders (c, d) for coarse powders. Cross sections are parallel (a and c) and perpendicular (b and d) to the main temperature gradient direction.

From these reconstructions, the inverse surface area per unit volume is calculated as S_v^{-1} = 48 µm for the foam created with the fine powder, and S_v^{-1} = 42 µm for the coarse-powder foam. For comparison, image analysis of transverse cross sections resulted in pore widths of 50 and 61 µm, respectively, for the two foams. While both measurement methods are relevant to the size of the dendritic macropores, they should be interpreted differently. The image analysis technique is a 2D measure, so it is an accurate measure of pore widths perpendicular to the section plane. Because S_v^{-1} is a 3D measure, it better represents the average size scale of all the features present in the foams. Also, the image analyses are performed on a section of the billet adjacent to the volume used for tomography at a shared surface, not on the tomography samples themselves. It has been previously shown that in these directionally freeze-cast titanium structures, pore width varies with distance from the heat sink.[11] Finally, Fig. 2 shows that pore width can also vary at the same distance from the heat sink.

The pore volume fractions differ significantly between the Archimedes and reconstruction measurements: 41.4% and 52% for the fine-powder foams and 44.6% and 63% for the coarse-powder foams. It is likely that this discrepancy is due to the resolution problem discussed earlier. It might also be due to varying pore volume fractions within the samples. Archimedes data is taken on a larger portion of the billet, so this value is a more accurate measure because it averages local variations. The 3D reconstructions are confined to a smaller volume—a volume of approximately 8 mm^3 is reconstructed here—compared to the billet's 62 mm^3 volume; therefore, it cannot provide the same averaging of data. Furthermore, the long dimensions of the macropores are

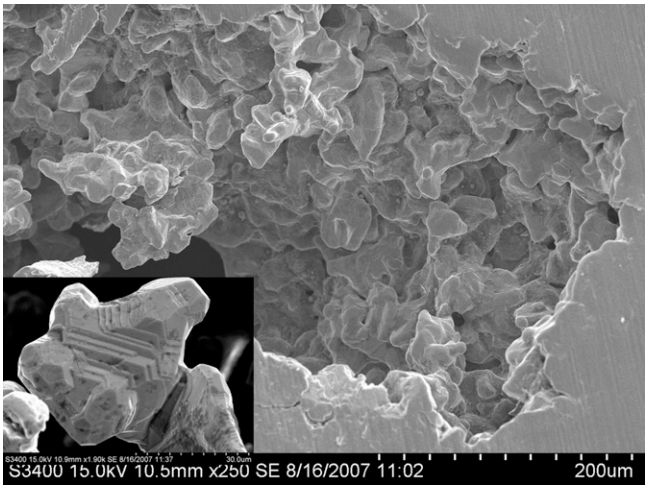

FIG. 3. SEM image of the parallel cross section of a macropore in titanium foam created by directional freeze-casting of coarse powders. Roughness and variation in curvature of the titanium walls are clearly visible at the scale of individual powders, and reflect the partially sintered state of the powders. Inset: Higher magnification SEM image showing partially sintered powder with ridges.

likely greater than the size of the tomography section leading to further inaccuracies.

The interconnectivity for the pore structures is also calculated and found to be 99.93% for both foams. This indicates that nearly all of the porosity within the reconstructed volumes is open porosity, in agreement with the pycnometric results.

Figures 5(a) and 5(b) show the ISDs for the two foams in this study. Two important features of the ISDs are the color bar and the axes of the plot. First, the minimum and maximum values of the color bar are fixed so that any differences in peak probability are clearly visible. Second, the principal curvatures shown on the axes are scaled by the characteristic length, S_v, to eliminate effects caused by a difference in the length scale due to varying powder sizes and pore volume fractions.

Two general observations can be drawn from these ISDs. First, the distributions, in both cases, are broad relative to S_v, which indicates a significant variation in the sizes of the pores in the structure. This can be explained by the fact that there are two different length scales in the foams: one corresponds to the dendritic, platelike macropores and the other corresponding to the equiaxed, closed micropores. Because the size scale of these micropores is on the same order as the resolution of the images, it most likely corresponds to the regions of small probability (purple) in both ISDs. Simply because of the small size scale of the micropores, and lack of spatial resolution used in the x-ray tomography technique, curvatures of $|\kappa/S_v| > 2$ are probably not adequately reconstructed and therefore an estimate at best. Second, both ISDs reside predominantly in regions 2 and 3, which encompass saddle-shaped or hyperbolic

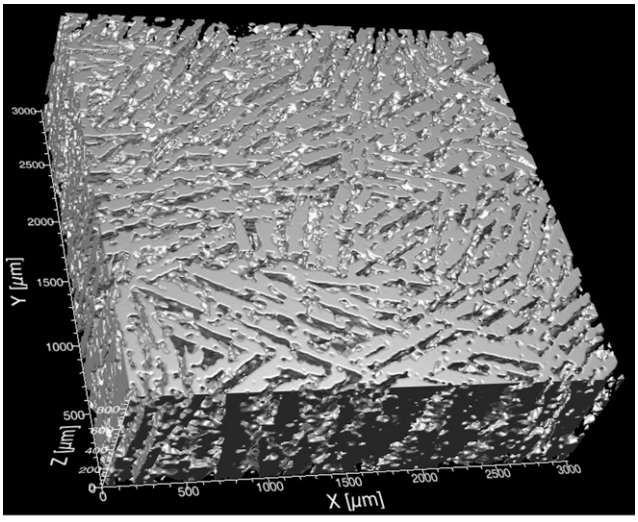

(a)

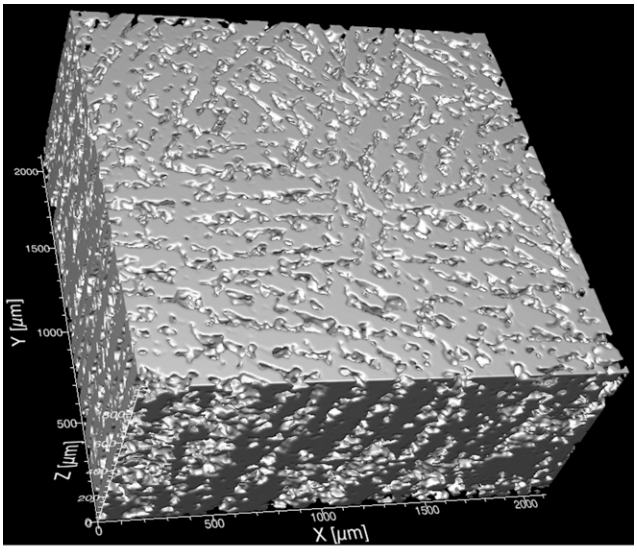

(b)

FIG. 4. Three-dimensional reconstructions of titanium foams: (a) for the fine powder and (b) for the coarse powder. To highlight the pore volumes, the titanium is transparent and the pores are displayed. The pore volume fractions for the samples are 52% and 63% for (a) and (b), respectively. The main ice growth direction is along the z axis.

interfaces. This corresponds directly with the roughness of the titanium walls caused from partially sintered individual powders. Almost all the surface patches have at least one negative principal curvature, κ_1, which is a result of the fact that over 75% of the surface patches have negative Gaussian curvature. This measure is comparable to what has been previously observed by Jinnai et al.[29,30] for trabecular bone microarchitecture, indicating that the processing technique used here could provide porous metallic implants that mimic bone with respect to distributions and percentages of curvatures in the microstructure.

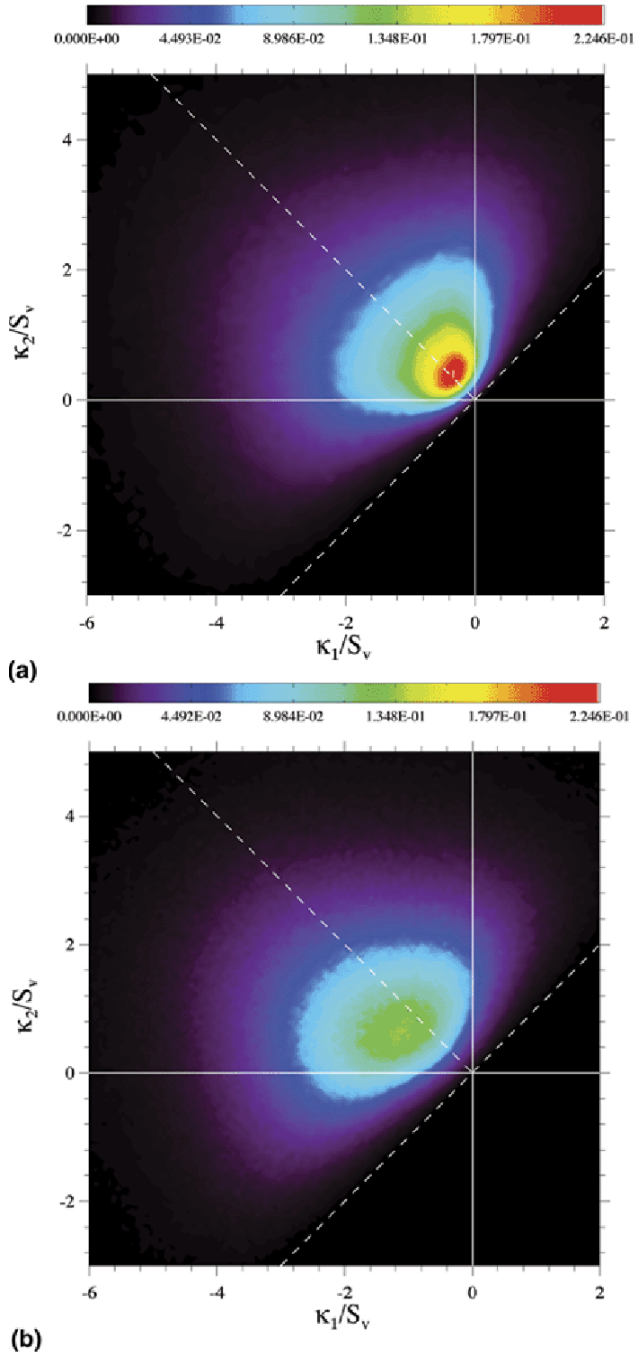

FIG. 5. Interface shape distributions of titanium foam samples created from: (a) a fine powder and (b) a coarse powder. (color online)

Comparing both ISDs, several observations can be made. The fine-powder foam has a well-defined peak whose center is located close to $\kappa_1/S_v = \kappa_2/S_v = 0$, indicating a higher probability of near-planar or flat interfaces in the microstructure. This corresponds to the platelike, titanium walls separating the pores produced by directional solidification. The distribution is also symmetrically located about the line $H = 0$, which is also a defining feature of the trabecular bone mentioned previously[30] and other bicontinuous structures.[31] The coarse-powder foam, on the other hand, does not exhibit as strong a peak as the fine-powder foam, and the center of its peak is located in region 3. The reason for the weaker peak is likely related to the degree of sintering. Assuming the ice dendrites grow identically with fine and coarse powders, the titanium walls between the ice dendrites should initially be the same width for each foam. However, because this width is not much larger than the powder size, the powder size can significantly affect how well the titanium packs into the interdendritic space during solidification, with the packing of the fine powders expected to be tighter. The improved initial packing and the increased driving force for sintering associated with the smaller powders then reduces the microporosity and the wall roughness in the sintered foam. This is supported by Fig. 2, which shows the fine-powder foam displaying fewer micropores and smoother, more well-defined titanium walls. By contrast, the coarse powders did not sinter as well, because of looser initial packing and lower driving force for sintering, resulting in titanium walls with more roughness and higher microporosity. Because ISDs are local measurements, the roughness in the walls may hide the overall planar structure present in the foam, resulting in a peak that is both weaker and shifted away from the line $H = 0$ and from the origin ($\kappa_1/S_v = \kappa_2/S_v = 0$).

To quantify preferential directionality in the titanium foams, we examine INDs (see Fig. 6). The near-hemisphere projection is provided for the fine-powder foam and the far-hemisphere projection is provided for the coarse-powder foam because the location of the individual peak values appears strongest in these projections. Because the results are qualitatively similar whether viewing the near- or far-hemisphere projections, it is important to use the hemisphere that contains the peak probability when comparing different structures. The z axis is chosen as the projection axis because it best displays the planar interfaces located in both structures. The minimum and maximum values of the color bars in the INDs are fixed based on the strongest directionality, observed in the fine-powder foam.

As a general observation, there is a significant distribution of normals surrounding the circumference of both INDs. In an ideal case, this would be representative of a perfect cylinder parallel to the projection axis, where the IND would reveal a thin stripe of equal probability encircling the outside of the projection. In the present case, it is representative of the platelike macropores parallel to the projection axis. The normals to the interfaces of these macropores are oriented randomly in the x-y plane but are still perpendicular to the solidification direction, z. Thus, the spread of probabilities is related to the imperfect alignment of the plates themselves, but the

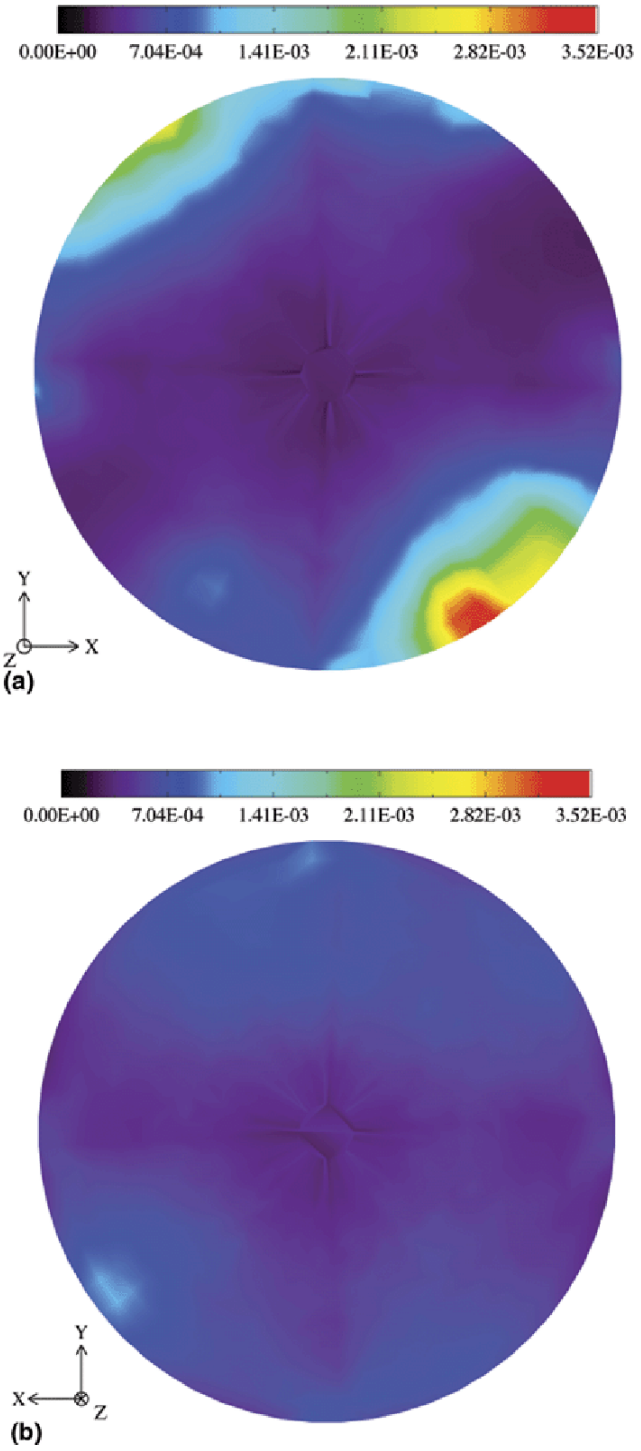

FIG. 6. Interface normal distributions of titanium foams formed with: (a) a fine powder and (b) a coarse powder. (color online)

location of the probabilities on the circumferences of the INDs indicate interfaces parallel to, or, equivalently, normals perpendicular to the growth direction, which results from the directional solidification process used to produce the samples. The two peaks located 180° apart in the IND for the fine-powder foam correspond to the more distinct platelike macropores in the microstructure that are apparent from general observations of the 2D micrographs and 3D reconstructions. The IND for the coarse-powder foam appears more isotropic in comparison to the IND for the fine-powder foam. This again can be explained by the degree of sintering in the structure. We would expect that the same directional solidification technique would produce a similar degree of anisotropy in the structure, but the wall roughness caused by incomplete sintering is most likely masking this anisotropy.

V. CONCLUSIONS

Two titanium foams, created by directional freeze-casting of two different sizes of titanium powders, were analyzed using synchrotron x-ray tomography to create 3D reconstructions. A quantitative morphological analysis was performed on these reconstructions, with the main results as follows:

(1) Aligned, elongated, platelike macropores, resulting from the removal of the directionally solidified ice dendrites, are easily resolved and reconstructed in three dimensions. Equiaxed micropores within the titanium walls separating macropores, which are due to incomplete sintering of the original powders, are close to the resolution of the present technique.

(2) The morphological differences of the pores in the two foams can be quantified by interfacial shape distributions (describing interfacial curvatures) and interface normal distributions (describing preferential directionality). These are useful tools in assessing variations in pore shape or orientation between the foams due to differences in processing conditions, e.g., powder size. In particular, it is apparent that the foams produced with the smaller powder size show more complete sintering, resulting in reduction of the undesirable microporosity without affecting the desirable dendritic macroporosity.

(3) Directional freeze-casting is a first step toward creating aligned, elongated pores mimicking the anisotropic pore structure of bone. Despite differences between this porous macrostructure and that of trabecular bone macroarchitecture, the morphology of the titanium foams shows similarities with bone on a local level.

ACKNOWLEDGMENTS

This research is supported by the Department of Energy Office of Basic Energy Science (Grant CNV0037736) and the National Science Foundation (Grant DMR0505772). J.L. Fife also gratefully acknowledges a National Science Foundation Graduate Research Fellowship. Part of this work was performed at the DuPont-Northwestern-Dow Collaborative Access Team

(DND-CAT) located at Sector 5 of the Advanced Photon Source (APS). DND-CAT is supported by E.I. DuPont de Nemours & Co., The Dow Chemical Company and the State of Illinois. Use of the APS was supported by the United States Department of Energy, Office of Science, Office of Basic Energy Sciences, under Contract No. DEAC0206CH11357. The authors thank Dr. Denis T. Keane for his invaluable assistance during the x-ray tomography experiments at APS.

REFERENCES

1. J. Banhart: Manufacture, characterisation and application of cellular metals and metal foams. *Prog. Mater. Sci.* **46,** 559 (2001).
2. V. Shapovalov: Porous metals. *MRS Bull.* **19,** 24 (1994).
3. E.D. Spoerke, N.G.D. Murray, H. Li, L.C. Brinson, D.C. Dunand, and S.I. Stupp: Titanium with aligned, elongated pores for orthopedic tissue engineering applications. *J. Biomed. Mater. Res., A* **84,** 402 (2008).
4. D.C. Dunand: Processing of titanium foams. *Adv. Eng. Mater.* **6,** 369 (2004).
5. A. Schuh, J. Luyten, R. Vidael, W. Honle, and T. Schmickal: Porous titanium implant materials and their potential in orthopedic surgery. *Materialwiss. Werkstofftech.* **38,** 1015 (2007).
6. H. Zhang and A.I. Cooper: Aligned porous structures by directional freezing. *Adv. Mater.* **19,** 1529 (2007).
7. S.I. Deville: Freeze-casting of porous ceramics: A review of current achievements and issues. *Adv. Eng. Mater.* **10,** 155 (2008).
8. D. Koch, L. Andresen, T. Schmedders, and G. Grathwohl: Evolution of porosity by freeze casting and sintering of sol-gel derived ceramics. *J. Sol-Gel Sci. Technol.* **26,** 149 (2003).
9. S.W. Sofie and F. Dogan: Freeze casting of aqueous alumina slurries with glycerol. *J. Am. Ceram. Soc.* **84,** 1459 (2001).
10. K. Araki and J.W. Halloran: Room-temperature freeze casting for ceramics with nonaqueous sublimable vehicles in the naphthalene-camphor eutectic system. *J. Am. Ceram. Soc.* **87,** 2014 (2004).
11. Y. Chino and D.C. Dunand: Directionally freeze-cast titanium with aligned, elongated pores. *Acta Mater.* **56,** 105 (2008).
12. C. Coleou, B. Lesaffre, J.B. Brzoska, and F. Flin: Three-dimensional snow images by x-ray microtomography. *Ann. Glaciol.* **32,** 75 (2001).
13. G.S. Do, Y. Sagara, M. Tabata, K. Kudoh, and T. Higuchi: Three-dimensional measurement of ice crystals in frozen beef with a micro-slicer image processing system. *Int. J. Refrig.* **27,** 184 (2004).
14. F. Flin, J.B. Brzoska, D. Coeurjolly, R.A. Pieritz, B. Lesaffre, C. Coleou, P. Lamboley, O. Teytaud, G.L. Vignoles, and J.F. Delesse: Adaptive estimation of normals and surface area for discrete 3D objects: Application to snow binary data from x-ray tomography. *IEEE Trans. Image Process.* **14,** 585 (2005).
15. F. Flin, J.B. Brzoska, B. Lesaffre, C. Coleou, and R.A. Piertitz: Three-dimensional geometric measurements of snow microstructural evolution under isothermal conditions. *Ann. Glaciol.* **38,** 39 (2004).
16. R. Mousavi, T. Miri, P.W. Cox, and P.J. Fryer: Imaging food freezing using x-ray microtomography. *Int. J. Food Sci. Technol.* **42,** 714 (2007).
17. J. Lambert, I. Cantat, R. Delannay, A. Renault, F. Graner, H.A. Glazier, I. Veretennikov, and P. Cloetens: Extraction of relevant physical parameters from 3D images of foams obtained by x-ray tomography. *Colloids Surf., A: Physicochem. Eng. Aspects* **263,** 295 (2005).
18. C. Monnereau and M. Vignes-Adler: Optical tomography of real three-dimensional foams. *J. Colloid Interface Sci.* **202,** 45 (1998).
19. H. Bart-Smith, A.F. Bastawros, D.R. Mumm, A.G. Evans, D.J. Sypeck, and H.N.G. Wadley: Compressive deformation and yielding mechanisms in cellular Al alloys determined using x-ray tomography and surface strain mapping. *Acta Mater.* **46,** 3583 (1998).
20. T. Dillard, F. N'guyen, E. Maire, L. Salvo, S. Forest, Y. Bienvenu, J.D. Bartout, M. Croset, R. Dendievel, and P. Cloetens: 3D quantitative image analysis of open-cell nickel foams under tension and compression loading using x-ray microtomography. *Philos. Mag.* **85,** 2147 (2005).
21. S.A. McDonald, P.M. Mummery, G. Johnson, and P.J. Withers: Characterization of the three dimensional structure of a metallic foam during compressive deformation. *J. Microsc.* **223,** 150 (2006).
22. A.H. Benouali, L. Froyen, T. Dillard, S. Forest, and F. N'guyen: Investigation on the influence of cell shape anisotropy on the mechanical performance of closed cell aluminium foams using microcomputed tomography. *J. Mater. Sci.* **40,** 5801 (2005).
23. D.A. Drew: Evolution of geometric statistics. *J. Appl. Math.* **50,** 649 (1990).
24. L. Guillaume, D. Florent, and B. Atilla: Constant curvature region decomposition of 3D-meshes by a mixed approach vertex-triangle. *J. WSCG* **12,** 245 (2004).
25. R. Mendoza, J. Alkemper, and P.W. Voorhees: The morphological evolution of dendritic microstructures during coarsening. *Metall. Mater. Trans. A* **34,** 481 (2003).
26. D. Kammer and P.W. Voorhees: The morphological evolution of dendritic microstructures during coarsening. *Acta Mater.* **54,** 1549 (2006).
27. S. Deville, E. Saiz, and A.P. Tomsia: Freeze casting of hydroxyapatite scaffolds for bone tissue engineering. *Biomaterials* **27,** 5480 (2006).
28. J.W. Moon, H.J. Hwang, M. Awano, and K. Maeda: Preparation of NiO–YSZ tubular support with radially aligned pore channels. *Mater. Lett.* **57,** 1428 (2003).
29. H. Jinnai, H. Watashiba, T. Kajihara, Y. Nishikawa, M. Takahashi, and M. Ito: Surface curvatures of trabecular bone microarchitecture. *Bone* **30,** 191 (2002).
30. H. Jinnai, Y. Nishikawa, M. Ito, S.D. Smith, D.A. Agard, and R. J. Spontak: Topological similarity of sponge-like bicontinuous morphologies differing in length scale. *Adv. Mater.* **14,** 1615 (2002).
31. Y. Kwon, K. Thornton, and P.W. Voorhees: Coarsening of bicontinuous structures via nonconserved and conserved dynamics. *Phys. Rev. E: Stat., Nonlinear, Soft Matter Phys.* **75,** 021120 (2007).